

## Research



**Cite this article:** Ahmadzadeh H, Rausch MK, Humphrey JD. 2018 Particle-based computational modelling of arterial disease. *J. R. Soc. Interface* **15**: 20180616. <http://dx.doi.org/10.1098/rsif.2018.0616>

Received: 14 August 2018  
Accepted: 25 October 2018

**Subject Category:**  
Life Sciences – Engineering interface

**Subject Areas:**  
biomechanics, bioengineering

**Keywords:**  
soft tissue, aortic dissection, smoothed particle hydrodynamics, Donnan swelling, glycosaminoglycans

**Author for correspondence:**  
H. Ahmadzadeh  
e-mail: [hossein.ahmadzadeh@yale.edu](mailto:hossein.ahmadzadeh@yale.edu)

Electronic supplementary material is available online at <https://dx.doi.org/10.6084/m9.figshare.c.4318598>.

# Particle-based computational modelling of arterial disease

H. Ahmadzadeh<sup>1</sup>, M. K. Rausch<sup>2</sup> and J. D. Humphrey<sup>1</sup>

<sup>1</sup>Department of Biomedical Engineering, Yale University, New Haven, CT, USA

<sup>2</sup>Departments of Aerospace Engineering and Engineering Mechanics and Biomedical Engineering, The University of Texas at Austin, Austin, TX, USA

HA, 0000-0002-2424-1867; MKR, 0000-0003-1337-6472; JDH, 0000-0003-1011-2025

Accumulated glycosaminoglycans (GAGs) can sequester water and induce swelling within the intra-lamellar spaces of the medial layer of an artery. It is increasingly believed that stress concentrations caused by focal swelling can trigger the damage and delamination that is often seen in thoracic aortic disease. Here, we present computational simulations using an extended smoothed particle hydrodynamics approach to examine potential roles of pooled GAGs in initiating and propagating intra-lamellar delaminations. Using baseline models of the murine descending thoracic aorta, we first calculate stress distributions in a healthy vessel. Next, we examine increases in mechanical stress in regions surrounding GAG pools. The simulations show that smooth muscle activation can partially protect the wall from swelling-associated damage, consistent with experimental observations, but the wall can yet delaminate particularly in cases of smooth muscle dysfunction or absence. Moreover, pools of GAGs located at different but nearby locations can extend and coalesce, thus propagating a delamination. These findings, combined with a sensitivity study on the input parameters of the model, suggest that localized swelling can alter aortic mechanics in ways that eventually can cause catastrophic damage within the wall. There is, therefore, an increased need to consider roles of GAGs in aortic pathology.

## 1. Introduction

Aortic dissections are responsible for significant morbidity and mortality. They manifest primarily in the thoracic aorta and are classified as Stanford type A (in the ascending aorta and arch, constituting approx. 67% of all dissections) or type B (in the descending thoracic aorta, constituting approx. 33%). The prevailing thought asserts that dissections initiate as an intimal tear that propagates into the medial layer by creating a false lumen that fills with blood from the true lumen [1–3]. This concept arose from *in vivo* imaging of pre-existing dissections and post-mortem histopathological examinations, also of pre-existing dissections. In neither case was the initiating event known. By contrast, we have observed intramural delaminations as they develop *in vitro*, under physiologic biaxial loading and in the absence of intimal defects, in multiple mouse models of thoracic aortic aneurysms and dissections (TAADs). In particular, descending thoracic aortic specimens from a model harbouring a conditional knock-out of type 1 transforming growth factor-beta receptor exhibit *in vivo* and *in vitro* delaminations, and histology reveals co-localization of pooled glycosaminoglycans (GAGs) with the delaminations [4]. A similar co-localization of intra-lamellar GAG pools and macroscopic delaminations is seen in the thoracic aorta of mice having a smooth muscle myosin heavy chain mutation, another model of TAADs [5]. These two examples are consistent with a hypothesis we put forth based on the distinct histopathologic characteristic of pooled GAGs in thoracic aortic samples from patients having diverse conditions that predispose to TAADs [6]. This hypothesis was recently supported by a careful study of aortic specimens from over 50 patients as well as from another mouse model of TAAD, the hypomorphic fibrillin-1 deficient mouse [7].

GAGs are highly negatively charged macromolecules that attract positive ions from the interstitial fluid, such as  $\text{Na}^+$ , to promote local electroneutrality, which in turn causes an influx of water molecules and creates a Gibbs–Donnan swelling pressure [8]. We suggest that, when localized by pooled GAGs, such swelling pressures can separate medial lamellae and thereby initiate a delamination that can propagate and lead to a dissection, that is, a physical connection with the lumen resulting in intramural blood flow or thrombus. Although we have observed delaminations using optical coherence tomography during *in vitro* biomechanical testing [4], such data provide only qualitative information. In this paper, we propose a new computational model to simulate GAG-induced intramural delaminations, including nucleation and propagation. Towards this end, we use a particle-based discretization for continuum mechanics, originally called smoothed particle hydrodynamics (SPH), that we extended to capture the nonlinear elasticity that characterizes normal soft tissue mechanics [9]. Specifically, we model the murine aorta in health and cases of intramural delamination driven by focal GAG-induced Gibbs–Donnan swelling.

## 2. Methods

### 2.1. Smoothed particle hydrodynamics for continuum mechanics

We define the computational domain by a collection of ordered ‘particles’ at which continuum quantities are transformed into discrete counterparts (figure 1a). Thus, these particles carry local mechanical information such as position, velocity, stress, and strain. Each particle is associated with a list of neighbouring particles, located within its interaction domain, and characterized by a kernel function that governs the locality and nature of particle interactions. For the Lagrangian formulation considered herein, particle locations ( $\mathbf{X}_i$  where  $i$  labels a particle) are defined in a physiologically and computationally convenient reference configuration wherein the list of neighbouring particles remains unchanged during a simulation. The Lagrangian formulation is convenient here because of our choice of reference configuration and the finding in pilot simulations that load-induced particle displacements do not dramatically change the geometry.

With proper choices of kernel functions and interaction domains, one can estimate the value of a continuous scalar function at any particle  $i$  by summing over its neighbouring particles ( $S$ ):

$$\hat{g}(\mathbf{X}_i) = \sum_{j \in S} g(\mathbf{X}_j) V_j \xi(R_j), \quad (2.1)$$

where  $\xi(R_j)$  is a kernel function centred at particle  $i$ , with  $R_j = |\mathbf{R}_j|$  the length of a reference position vector,  $\mathbf{R}_j = \mathbf{X}_j - \mathbf{X}_i$ , between any two particles including  $i$ . The approximation is also weighted by the ‘volume’ of the neighbouring particles, denoted by  $V_j$  and defined by the area enclosed by neighbouring particles in the  $r - \theta$  plane multiplied by the fixed axial stretch in the  $z$  direction.

Referential gradients of these scalar functions are calculated as

$$\nabla_{\mathbf{X}} \hat{g}(\mathbf{X}_i) = \sum_{j \in S} g(\mathbf{X}_j) V_j \nabla_{\mathbf{X}} \xi(R_j), \quad (2.2)$$

with the gradient of the kernel function given by

$$\nabla_{\mathbf{X}} \xi(R_j) = \left( \frac{\partial \xi(R_j)}{\partial R_j} \right) \frac{\mathbf{R}_j}{R_j}. \quad (2.3)$$

We use a third-order polynomial function  $\xi(R_j)$ , known as Spiky kernel [10], which has a derivative that attenuates with inter-particle distance (figure 1b):

$$\xi(R_j) = \begin{cases} \frac{10(h - R_j)^3}{\pi h^5} & R_j < h, \\ 0 & R_j \geq h, \end{cases} \quad (2.4)$$

where the smoothing parameter  $h$  defines the kernel support (figure 1b) and the pre-factor  $10/(\pi h^5)$  normalizes the kernel function in a two-dimensional ( $r - \theta$ ) space. Note that this kernel function, centred at particle  $j$ , is radially symmetric and depends only on the distance between particles; this symmetry defines the interaction domain, not the geometric or material symmetries that are defined by the overall computational domain and constitutive relations, respectively.

Completeness of a numerical approximation is defined as the highest order polynomial function that can be captured exactly by the model. Zeroth-order and first-order completeness conditions can be written [11]

$$\sum_{j \in S} V_j \xi(R_j) = 1, \quad \sum_{j \in S} V_j \nabla_{\mathbf{X}} \xi(R_j) = 0. \quad (2.5)$$

In SPH, zeroth-order completeness of the derivative of a function is achieved by symmetrizing the derivatives [9,12]

$$\nabla_{\mathbf{X}} \hat{g}(\mathbf{X}_i) = \sum_{j \in S} V_j (g(\mathbf{X}_j) - g(\mathbf{X}_i)) \nabla_{\mathbf{X}} \xi(R_j); \quad (2.6)$$

first-order completeness is achieved by introducing a correction matrix in the definition of the derivative of the kernel function, such that [11]

$$\sum_{j \in S} \mathbf{R}_j \otimes V_j \tilde{\nabla}_{\mathbf{X}} \xi(R_j) = \mathbf{I}, \quad (2.7)$$

with the corrected gradient  $\tilde{\nabla}_{\mathbf{X}} \xi(R_j)$ , depending on a correction matrix (denoted by  $\mathbf{A}_i$ ), given by

$$\left. \begin{aligned} \tilde{\nabla}_{\mathbf{X}} \xi(R_j) &= \mathbf{A}_i^{-1} \nabla_{\mathbf{X}} \xi(R_j) \\ \text{and } \mathbf{A}_i &= \sum_{j \in S} V_j \nabla_{\mathbf{X}} \xi(R_j) \otimes \mathbf{R}_j. \end{aligned} \right\} \quad (2.8)$$

Observe that a vector  $\mathbf{a}$  or tensor  $\mathbf{A}$  evaluated for a particle  $i$  that was originally at  $\mathbf{X}_i$  is denoted by  $\mathbf{a}_i$  and  $\mathbf{A}_i$ , respectively. Hence, the operators  $\otimes$  and  $\cdot$  denote the usual dyadic and dot product of two vectors ( $\mathbf{a}_i \otimes \mathbf{a}_j = a_{ik} a_{jl} \mathbf{e}_k \otimes \mathbf{e}_l$  and  $\mathbf{a}_i \cdot \mathbf{a}_j = a_{i1} a_{j1} + a_{i2} a_{j2} + a_{i3} a_{j3}$ ), and double contraction of two tensors is defined as  $\mathbf{T}_i : \mathbf{T}_j = \text{tr}(\mathbf{T}_i^T \mathbf{T}_j)$ .

### 2.2. Implementation for hyperelastic materials

The deformation gradient is defined as  $\mathbf{F}_i = \partial \mathbf{x} / \partial \mathbf{X}_i$ , where  $\mathbf{X}$  and  $\mathbf{x}$  are referential and current positions of individual particles, here particle  $i$ . Using equations (2.6) and (2.8), we have

$$\mathbf{F}_i = \sum_{j \in S} \mathbf{r}_j \otimes V_j \tilde{\nabla}_{\mathbf{X}} \xi(R_j), \quad (2.9)$$

where  $\mathbf{r}_j = \mathbf{x}_j - \mathbf{x}_i$  is the position vector between two particles in the current configuration (including  $i$ ) with length  $r_j$ . Defining the right Cauchy–Green tensor  $\mathbf{C}_i = \mathbf{F}_i^T \mathbf{F}_i$ , and assuming a hyperelastic material behaviour, we can determine the second Piola–Kirchhoff stress ( $\mathbf{S}_i$ ), first Piola–Kirchhoff stress ( $\mathbf{P}_i$ ) and

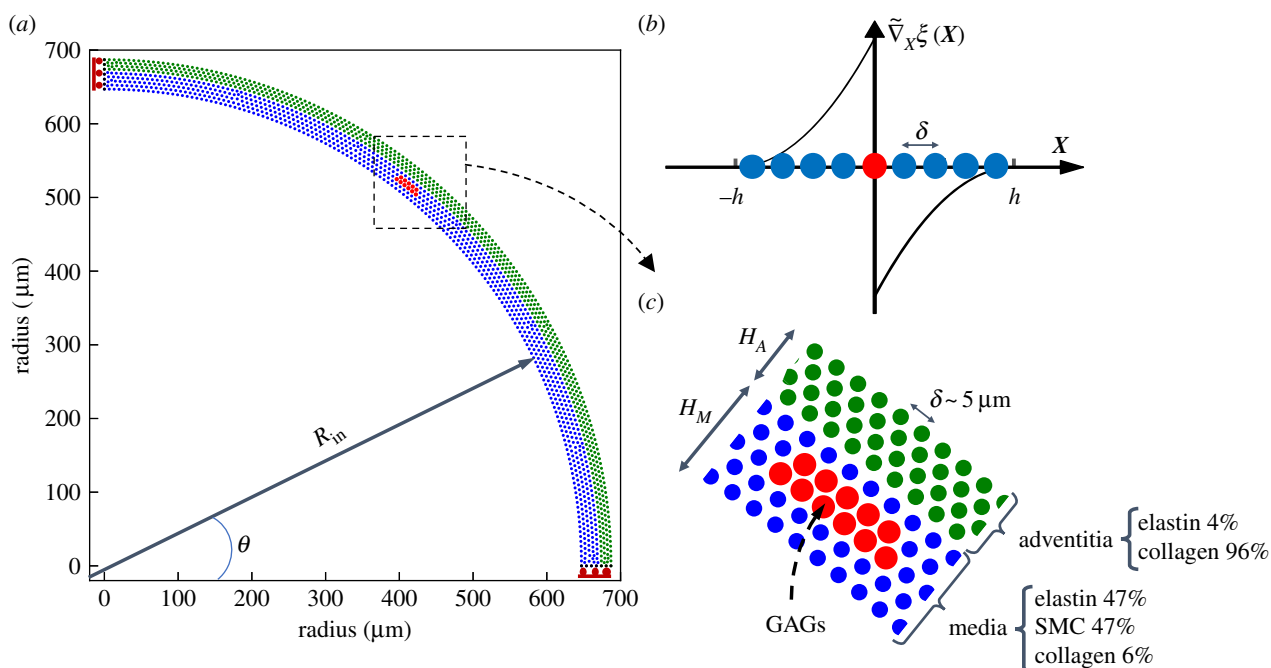


**Figure 1.** SPH model of a bi-layered murine aorta in its reference configuration. (a) Arrangement of particles, accounting for adventitia (green), normal media (blue), and GAGs (red). The quarter-symmetric domain is bounded between two sliding boundaries. (b) A one-dimensional demonstration of the derivative of the kernel function reveals that the repelling force between two particles increases as they approach each other; note, too, the kernel support with respect to the spacing of the particles. (c) Material composition of each layer and the associated mass fractions (%) for elastin, collagen fibres and SMCs as well as a pool of GAGs within the media.

Cauchy stress ( $\sigma_i$ ) tensors by

$$S_i = 2 \frac{\partial W(C_i)}{\partial C_i}, \quad P_i = F_i S_i, \quad \sigma_i = \frac{1}{J_i} P_i F_i^T. \quad (2.10)$$

Here,  $J_i$  is the volume change associated with particle  $i$  (i.e. the volume enclosed by its interacting neighbours).

Following Ganzenmüller [11], the internal force exerted on the particle originally located at  $X_i$  is

$$f_i^{\text{int}} = \sum_{j \in S} f_{ij} = \sum_{j \in S} V_i V_j (P_i \tilde{\nabla}_X \xi(R_j) - P_j \tilde{\nabla}_X \xi(R_i)), \quad (2.11)$$

where  $V_i$  and  $V_j$  are volumes associated with the central particle and its neighbours, respectively. Once the internal force exerted on the particles is defined, the acceleration of a particle is calculated by satisfying linear momentum balance:

$$f_i^{\text{int}} + f_i^{\text{ext}} = m_i \ddot{x}_i, \quad (2.12)$$

with  $f_i^{\text{ext}}$  denoting external forces acting on the particle and  $m_i$  denoting its mass.

Assuming a constant time interval  $\Delta t$ , we use the leapfrog time integration scheme and determine spatial positions of the particles for all times  $t \geq 1$  via

$$x_i^t = x_i^{t-1} + v_i^{t-1/2} \Delta t \quad (2.13a)$$

and

$$v_i^{t+1/2} = v_i^{t-1/2} + \ddot{x}_i^t \Delta t, \quad (2.13b)$$

with  $v_i^{1/2} = \dot{x}_i^0 \Delta t / 2$ , noting that  $x_i^0 \equiv X_i$  are the referential coordinates.

### 2.3. Mechanical stabilization

The basic SPH formulation can be susceptible to instabilities arising from a rank-deficiency, which induces non-physical, zero-energy modes. To achieve stable simulations, we adopt an approach proposed by Ganzenmüller [11] that mimics hourglass

control used in finite-element methods wherein a penalty force (denoted by  $f_i^{\text{hg}}$ ) is added to the particle forces, namely

$$f_i^{\text{hg}} = \sum_{j \in S} -\alpha \frac{E V_i V_j \xi(R_j)}{2R_j^2} (\delta_i + \delta_j) \frac{r_j}{r_j}. \quad (2.14)$$

Here,  $E$  is the hourglass stiffness, analogous to Young's modulus, and  $\alpha$  is a control parameter chosen via a sensitivity study (e.g.  $\alpha = 5 - 100$  [11]). Finally, the length parameters are defined as

$$\delta_i = \frac{(F_i R_j - r_j) r_j}{r_j}. \quad (2.15)$$

We can further stabilize particle motions by introducing an artificial viscosity to dissipate spurious oscillations in interactions between particles. Using the stretching tensor  $d_i = (l_i + l_i^T)/2$ , where the spatial velocity gradient is  $l_i = \dot{F}_i F_i^{-1}$  and the rate of change of the deformation gradient is  $\dot{F}_i = (F_i^{t+1} - F_i^t)/\Delta t$ , the viscous first Piola–Kirchhoff stress tensor,  $P_i^{\text{visc}} = 2\eta_j d_i F_i^{-T}$ , is added to  $P_i$  in equation (2.10), where the viscosity  $\eta$  is determined parametrically. This addition does not affect the final quasi-static results.

### 2.4. Arterial models

Assuming axisymmetry of an idealized cylindrical aorta, a good approximation of the normal descending thoracic aorta in the mouse, let a quarter-circle domain represent the cross section, with inner and outer radii  $R_{\text{in}}$  and  $R_{\text{out}}$  and wall thickness  $H$  defined in the reference configuration ( $t = 0$ ). Boundary conditions at the vertical and horizontal edges of the quarter-circle are given by a sliding displacement vector (figure 1a). Any point in the deformed configuration is given by  $(r, \theta, z)$ , where  $\theta = 0$  and  $\theta = \pi/2$  correspond to horizontal and vertical boundaries.

Before considering effects due to local swelling pressures caused by pooled GAGs, consider two baseline computational models that define the homeostatic configuration and associated stresses and stretches. The first (mean-behaviour) model is based

on data obtained from biaxial mechanical tests wherein the murine aorta is held at a fixed axial length and distended by increasing the intraluminal pressure while recording changes in outer diameter [13]. Given that pressure–diameter data only reveal bulk behaviours, this model does not delineate layers of the wall (i.e. stresses and strains are averaged transmurally). The second model is bi-layered to represent the media and adventitia, each homogenized but otherwise defined by appropriate material compositions for each layer. In addition to capturing the same pressure–diameter behaviour, this model better predicts the transmural distribution of stress as well as characteristics such as residual stresses in a traction-free state (zero pressure and axial force).

#### 2.4.1. Mean-behaviour smoothed particle hydrodynamics model

The mean circumferential stress experienced by an artery is

$$\sigma_\theta = \frac{Pr_{in}}{h}, \quad (2.16)$$

where  $r_{in}$  and  $h$  denote the inner radius and wall thickness at distending pressure  $P$ . The associated circumferential stretch is

$$\lambda_\theta = \frac{r_{in} + h/2}{R_{in} + H/2}. \quad (2.17)$$

Based on prior constitutive descriptions of biaxial data for the proximal descending thoracic aorta of a mouse [14], we adopt a strain energy function  $W$  that models the homogenized roles of nearly circularly oriented passive smooth muscle cells (SMCs) as well as elastin- and collagen-dominated extracellular matrix [13], evaluated particle-wise,

$$W(C_i, \mathbf{M}_i^k) = \frac{\mu}{2}(I_{1i} - 3 + \ln J_i) + \frac{\hat{\lambda}}{2}(\ln J_i)^2 + \sum_{k=1}^4 \frac{c_k^k}{4c_k^k} (\exp[c_2^k(I_{4i}^k - 1)^2] - 1). \quad (2.18)$$

The first two terms account for the nearly isotropic elastin-dominated behaviour, modelled as a neo-Hookean solid with  $I_{1i} = \text{tr}(C_i)$  and  $\mu$  and  $\hat{\lambda}$  the shear modulus and Lamé parameter, respectively. Note that this form does not represent a fully incompressible material behaviour, as traditionally used to model soft tissues. The Jacobian of the deformation gradient,  $J_i = \det(\mathbf{F}_i^{2D})\lambda_{zi}$ , represents possible volume changes by accounting for area changes, in the two-dimensional domain (through  $\det(\mathbf{F}_i^{2D}) = F_{11}F_{22} - F_{12}F_{21}$ ) plus the stretch in the axial direction ( $\lambda_{zi}$ ), with an ‘effective’ Poisson’s ratio proportional to  $\sim \hat{\lambda}/\mu$ , which can be rendered close to 0.5 by considering a relatively large  $\hat{\lambda}/\mu \approx 100$  to 1000 (resulting in the Poisson’s ratio 0.495–0.499). The last term in equation (2.18) accounts for the collective behaviour of the collagen-dominated matrix and embedded SMCs via four locally parallel families, including axial ( $k = 1$ ), circumferential ( $k = 2$ ) and two symmetric diagonal ( $k = 3, 4$ ) families. The SMC contributions are added to that of the circumferential family of collagen fibres ( $k = 2$ ) because the two cannot be delineated with current experimental data and this constitutive model is structurally motivated, yet phenomenological in that it fits biaxial data well without attempting to account for constituent-to-constituent interactions [15]. Based on these definitions,  $I_{4i}^k$  denotes the square of the stretch associated with the  $k$ th family, namely

$$I_{4i}^k = \mathbf{C}_i : \mathbf{M}_i^k \otimes \mathbf{M}_i^k, \quad (2.19)$$

where  $\mathbf{M}_i^k = [0, \sin \alpha, \cos \alpha]$  is a unit vector in the direction of family  $k$  at particle  $i$ , with  $\alpha = 0, 90$  for axial and circumferential families and  $\alpha = \pm \alpha_0$  ( $0 < \alpha_0 < 90$ ) for the diagonal families. Finally,  $c_1^k$  and  $c_2^k$  are material constants, which are listed in table 1 with other geometric and mechanical parameters.

**Table 1.** Parameters used in the mean-behaviour SPH model, adapted from [14]. Contributions of SMCs and circumferentially oriented collagen fibres ( $k = 2$ ) are considered together.

parameter	symbol	value
inner and outer radii (unloaded)	$R_{in}, R_{out}$	332 $\mu\text{m}$ , 444 $\mu\text{m}$
elastin-dominated material constant	$\mu$	18.53 kPa
axial collagen parameters	$c_1^{k=1}, c_2^{k=1}$	25.370 kPa, 0.036
SMC + circumferential collagen parameters	$c_1^{k=2}, c_2^{k=2}$	16.593 kPa, 0.108
diagonal collagen parameters	$c_1^{k=3,4}, c_2^{k=3,4}, \alpha_0$	0.078 kPa, 1.719, 28.783°
axial stretch	$\lambda_z$	1.62

Consequently, the second Piola–Kirchhoff stress tensor  $\mathbf{S} = 2\partial W(C)/\partial C$  is

$$\mathbf{S}_i = \mu_0(\mathbf{I} - \mathbf{C}_i^{-1}) + \frac{\hat{\lambda}}{2} \ln J_i \mathbf{C}_i^{-1} + \sum_{k=1}^4 c_1^k (I_{4i}^k - 1) \exp[c_2^k (I_{4i}^k - 1)^2] \mathbf{M}_i^k \otimes \mathbf{M}_i^k. \quad (2.20)$$

To achieve the homeostatic configuration, we apply a uniform axial stretch ( $\lambda_z = 1.62$ ) and distend the artery by increasing the luminal pressure to 103 mmHg while calculating pressure–diameter and circumferential stress–stretch behaviours. At  $t_0 = 0$ , we set  $\mathbf{F}_i^{t_0} = \mathbf{I}$  and  $\lambda_{zi}^{t_0} = 1$ , resulting in  $J_i^{t_0} = 1$  and  $\mathbf{S}_i^{t_0} = 0$  for all particles. We update the axial stretch at  $t_1 = t_0 + \Delta t$  such that  $\lambda_{zi}^{t_1} = \lambda_{zi}^{t_0} + \Delta \lambda_z$ , where  $\Delta \lambda_z$  is an incremental extension experienced by all particles over a time step, which leads to  $J_i^{t_1} \neq 1$  and  $\mathbf{S}_i^{t_1} \neq 0$  from equation (2.20). This non-zero stress translates to non-zero forces that eventually move the particles such that the total strain energy (in equation (2.18)) is minimized and  $J_i^{t_1} = 1$ . We subsequently increase the axial stretch and repeat this process until achieving the desired value ( $\lambda_z = 1.62$  in table 1). We then set  $\lambda_z = 1.62$  in equation (2.20) and continue the simulations under plane strain. Figure 2a shows details of the computational algorithm.

To achieve a traction-free boundary condition on the outer surface, the first Piola–Kirchhoff stress is rotated to the direction of the surface normal defined in the reference configuration and the normal component corresponding to the radial stress is set to zero. To determine the outer diameter at different intraluminal pressures, we simply distend the artery by applying the appropriate displacement boundary condition on the inner surface and calculate the corresponding pressure from equations (2.16) and (2.17). Performing a relaxation step at the final time step dissipates oscillations of the particles to achieve a true quasi-static configuration. One such relaxation step is shown in electronic supplementary material, figure S1, where oscillations in outer radius of an artery are shown for an increase in pressure to a new fixed value.

#### 2.4.2. Bi-layered smoothed particle hydrodynamics model

Pressurizing the mean-behaviour arterial model at a fixed axial stretch (plane strain mode) will reproduce the measured biaxial pressure–diameter data. Nonetheless, a tacit assumption of this

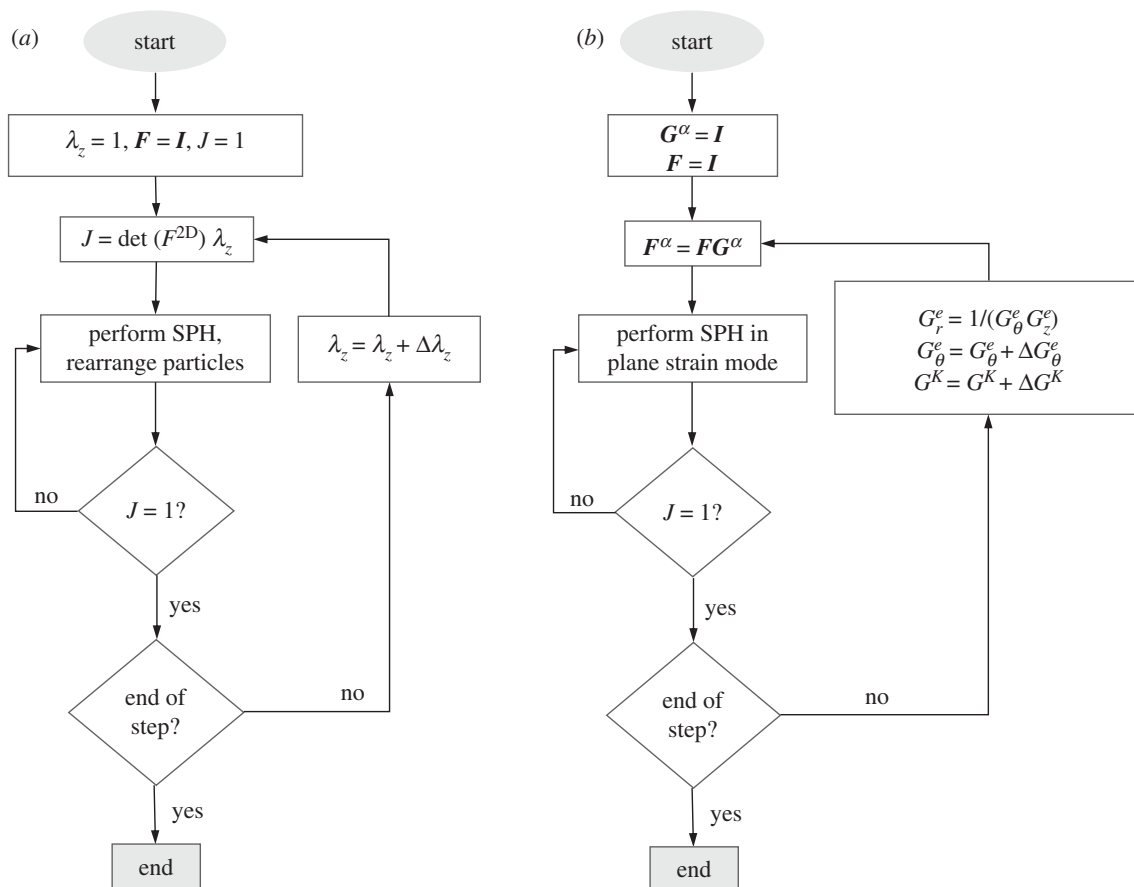


**Figure 2.** Algorithms that introduce (a) axial stretch in the mean-behaviour model or (b) constituent-specific deposition pre-stretches in the bi-layered model.

model is that the intact artery is initially stress-free when traction-free. This assumption is by contrast with observations from ‘opening angle’ experiments. Notably, introducing a radial cut across the wall in the traction-free configuration induces an ‘opening up’ to a sector to relieve residual stresses [16]. To incorporate residual stresses, one can start the simulations from a radially cut, traction-free configuration and then, by introducing appropriate displacement boundary conditions at the open ends, close the artery to induce the residual stresses [16]. While this approach has been successful in analytical and mesh-based (finite element) studies [17], similar implementation in particle-based methods necessitates special consideration. In particular, closing an open sector alters the relative angles between the particles and their neighbours. Given the Lagrangian framework of our SPH method and because the neighbours and their coordinates are typically defined in a stress-free reference configuration, our preliminary simulations suggested that disturbing the relative angles can reduce numerical stability and eventually lead to inaccurate solutions. This issue is even more acute when some constituents, such as collagen fibres and SMCs, have directional behaviour and depend strongly on the relative angles between particles. Thus, we adopted a different approach [15]. Instead of defining stress-free or traction-free configurations as a reference, we start our simulations from the homeostatic *in vivo* configuration and introduce ‘deposition pre-stretches’ specific to each constituent to capture the initial homeostatic stress field. These pre-stretches define mappings between the natural (stress-free) configuration for each constituent and the reference *in vivo* configuration of the vessel. Pre-stretches arise from developmental stresses (such as the stretch of elastic fibres due to somatic growth) and especially cell-mediated deposition pre-stresses (e.g. cells deposit collagen fibres within extant matrix with an initial stress) [18]. Finally, we create a bi-layered model (accounting for media and adventitia) and assign histologically derived

mass fractions for elastic fibres, collagen fibres, and SMCs in each layer (figure 1c).

The net deformation gradients are set to  $F_i = I$  in the homeostatic reference configuration, while the constituents experience deformation gradients associated with the prescribed deposition pre-stretches ( $F_i^\alpha = G_{\Gamma_i}^\alpha$ ), where  $G_{\Gamma_i}^\alpha$  denotes deposition pre-stretches for elastin-dominated matrix ( $\alpha = e$ ), combined SMCs and circumferential collagen fibres ( $\alpha = k$ ) in media ( $\Gamma = M$ ), or adventitia ( $\Gamma = A$ ). At non-homeostatic states,  $F_i^\alpha = F_i G_{\Gamma_i}^\alpha$ , where  $F_i$  denotes the deformation gradient corresponding to mappings from the reference homeostatic to a non-homeostatic configuration. Similar to the mean-behaviour model, we use a neo-Hookean strain energy function to model the isotropic behaviour of the elastin-dominated matrix, namely

$$W^e(F_i^e) = \frac{\mu}{2}(I_{1i}^e - 3 + \ln J_i) + \frac{\hat{\lambda}}{2}(\ln J_i)^2. \quad (2.21)$$

Here  $I_{1i}^e = \text{tr}(C_i^e)$ , and  $C_i^e = (F_i^e)^T F_i^e$  is the right Cauchy–Green tensor for the elastin-dominated matrix with  $F_i^e = F_i G_{\Gamma_i}^e$ . Note that the Jacobian of the deformation gradient is defined as  $J_i = \det(F_i^e) \lambda_z$ , and given that  $\det(G_{\Gamma_i}^e) = 1$ , we obtain  $J_i = \det(F_i^{2D}) \lambda_z$ .

Similar to the mean-behaviour model, the collective contributions of the circumferentially oriented SMCs and four families of the collagen fibres (which physically are supported by aggregating GAGs and thus can support compression [15]) are modelled as

$$W^k(M_i^k) = \left. \begin{aligned} & \frac{c_1^{k+}}{4c_2^{k+}} \left( \exp \left[ c_2^{k+} ((I_{4i}^k)^2 - 1) \right] - 1 \right) I_{4i}^k \geq 1 \\ & \text{and } W^k(M_i^k) = \frac{c_1^{k-}}{4c_2^{k-}} \left( \exp \left[ c_2^{k-} ((I_{4i}^k)^2 - 1) \right] - 1 \right) I_{4i}^k < 1, \end{aligned} \right\} \quad (2.22)$$

**Table 2.** Parameters used in the bi-layered SPH model, adapted from [19], but including active properties.

parameter	symbol	value
inner and outer radii (homeostatic), media and adventitia thickness	$R_{in}, R_{out}$ $H_M, H_A$	646.8 $\mu\text{m}$ , 687.0 $\mu\text{m}$ , 28.4 $\mu\text{m}$ , 11.8 $\mu\text{m}$
elastin-dominated material constant	$\mu$	89.71 kPa
medial axial and diagonal collagen parameters (in tension + and compression -)	$c_1^{k=1,3,4+}, c_2^{k=1,3,4+}, \alpha_0$	234.9 kPa, 4.08
adventitial axial, circumferential and diagonal collagen parameters (in tension + and compression -)	$c_1^{k=1,3,4-}, c_2^{k=1,3,4-}$ $c_1^{k=1,2,3,4+}, c_2^{k=1,2,3,4+}, \alpha_0$ $c_1^{k=1,2,3,4-}, c_2^{k=1,2,3,4-}$	29.91° 29.14 kPa, 4.08
medial SMC + circumferential collagen parameters (in tension + and compression -)	$c_1^{k=2+}, c_2^{k=2+}$ $c_1^{k=2-}, c_2^{k=2-}$	261.4 kPa, 0.24 249.5 kPa, 0.15
medial mass fractions	$\phi_M^e, \phi_M^s, \phi_M^{c_{1,3,4}}$	0.47, 0.47, 0.06
adventitial mass fractions	$\phi_A^e, \phi_A^{c_{1,2,3,4}}$	0.04, 0.96
medial collagen orientations	$\beta_M^z, \beta_M^d$	0.056, 0.944
adventitial collagen orientations	$\beta_A^z, \beta_A^d, \beta_A^\theta$	0.067, 0.877, 0.056
medial and adventitial elastin deposition pre-stretch	$G_{\Gamma,r}^e, G_{\Gamma,\theta}^e, G_{\Gamma,z}^e$	0.32, 1.90, 1.62
medial SMC + circumferential collagen deposition pre-stretch	$G_M^{k=2}$	1.20
medial and adventitial collagen deposition pre-stretch	$G_M^{k=1,3,4}, G_A^{k=1,2,3,4}$	1.25
circumferential stretch with maximum and minimum active stress	$\lambda_{max}$ $\lambda_{min}$	1.1 0.6
applied stimulus of the active tone	$T_{max}$	258 kPa

where  $I_{4i}^k$  is the square of the stretch defined as  $I_{4i}^k = G_{\Gamma i}^k \sqrt{C_i : M_i^k \otimes M_i^k}$ .

Finally, given that the collagen/SMC dominated behaviour exhibits higher stiffness in response to tensile compared to compressive loading, their behaviour is modelled by two sets of material parameters:  $(c_1^{k+}, c_2^{k+})$  for tension and  $(c_1^{k-}, c_2^{k-})$  for compression. This strain energy also accounts for the histology-derived averaged mass fraction for each constituent (figure 1c):  $\phi_\Gamma^e$  for elastin in media ( $\Gamma = M$ ) or adventitia ( $\Gamma = A$ ) and  $\phi_\Gamma^c$  for the mass fractions of the four families of collagen fibres ( $k = 1, 2, 3, 4$ ) within the media ( $\Gamma = M$ ) or adventitia ( $\Gamma = A$ ). Note that  $\phi_M^{c_2}$  includes the circumferentially oriented SMCs in the media. In addition, to distinguish further the collagen in different directions, we multiply the defined mass fractions ( $\phi_M^{c_{1,3,4}}, \phi_A^{c_{1,2,3,4}}$ ) by an appropriate scaling factor ( $\beta_\Gamma^z, \beta_\Gamma^d, \beta_\Gamma^\theta$ ) and obtain the content of the collagen in the axial ( $z$ ), circumferential ( $\theta$ ) and diagonal ( $d$ ) directions [15]. Note that  $\beta_M^z + \beta_M^d = 1$  and  $\beta_A^z + \beta_A^d + \beta_A^\theta = 1$ . The parameters of the bi-layered model are given in table 2 [19].

Altogether, the local strain energy function of the bi-layered system is defined as

$$W(C_i, M_i^k) = \phi_{M,A}^e W^e(F_i^e) + \sum_{k=1}^4 \phi_\Gamma^c W^c(I_{4i}^k). \quad (2.23)$$

To build-in constituent-specific deposition pre-stretches, we start from the homeostatic configuration at  $t_0 = 0$  and set  $F_i^{t_0} = \mathbf{I}$  and  $G_i^\alpha = \mathbf{I}$  whereby  $S_i^{\alpha_0} = 0$  and internal forces  $f_i^{\text{int}}(t_0) = 0$ . We next pre-stretch each constituent such that  $G_i^\alpha(t_1) = G_i^\alpha(t_0) + \Delta G^\alpha$ , where  $\Delta G^\alpha$  denotes an incremental increase in deposition pre-stretch over one time step at particle  $i$ , with  $G_r^e = 1/(G_\theta^e G_z^e)$  for the amorphous elastin-dominated material, leading to

$F_i^\alpha = F_i^{t_1} G_i^\alpha \neq \mathbf{I}$  and accordingly,  $S_i^{t_1} \neq 0$  and  $f_i^{\text{int}}(t_1) \neq 0$ . As further simulations proceed in a plane strain configuration, the load-induced axial stretch in equation (2.21) remains as  $\lambda_z \equiv 1$  despite the overall axial stretch being homeostatic. By enforcing a constrained displacement boundary condition on the inner surface and imposing (near) incompressibility through a large  $\hat{\lambda}/\mu$  in equation (2.21), movement of the particles is suppressed and internal stresses arise with the defined pre-stretches. By repeating this process for additional time steps, the model finally adopts the homeostatic state of the stresses while preserving geometrical characteristics such as inner radius and thickness.

## 2.5. Active stress of the smoothed particle hydrodynamics

Active stress generated by SMC contractility is assumed to act along the orientation of the cells in the circumferential direction. Following [20], the following active Cauchy stress is added to the circumferential stress of the medial particles:

$$\sigma_\theta^{\text{act}} = T_{max} \lambda_\theta \left[ 1 - \left( \frac{\lambda_{max} - \lambda_\theta}{\lambda_{max} - \lambda_{min}} \right)^2 \right]. \quad (2.24)$$

Note that this active stress reaches its maximum value when the circumferential stretch ( $\lambda_\theta$ , with respect to the reference configuration of the passive model) equals  $\lambda_{max}$  and it vanishes at stretch  $\lambda_{min}$ .  $T_{max}$  is a parameter that regulates the maximum value of active stress and generally depends on the applied stimulus (e.g. vasoagonist).  $T_{max}$ ,  $\lambda_{max}$  and  $\lambda_{min}$  are determined such that full contraction of the SMCs induces a nearly 20% reduction in the outer diameter of the artery at the homeostatic pressure (103 mmHg), in agreement with measurements for the descending thoracic aorta of mouse [21].

## 2.6. Gibbs–Donnan swelling caused by pooled GAGs

Swelling pressures caused by a medial pool of GAGs are calculated and applied as an additional term in the Cauchy stress tensor. By assuming an ideal solution, the osmotic pressure ( $\Pi$ ) due to the presence of ions is

$$\Pi = RT(c^+ + c^- - c^*), \quad (2.25)$$

with  $c^+$  and  $c^-$  the concentration of ions within the arterial wall (such as  $\text{Na}^+$  and  $\text{Cl}^-$ ) and  $c^*$  the ionic concentration of the surrounding medium;  $R$  and  $T$  are the gas constant and the absolute body temperature (310K). In the presence of immobile ‘fixed charged’ macromolecules (FC), such as GAGs, the concentration of the positive and negative ions within the arterial wall is determined by the Gibbs–Donnan equation:

$$c^+ + c^- = \sqrt{(c^{\text{FC}})^2 + (c^*)^2}, \quad (2.26)$$

where  $c^{\text{FC}}$  is the concentration of the GAGs. Hence, the osmotic pressure is  $\Pi = RT\left(\sqrt{(c^{\text{FC}})^2 + (c^*)^2} - c^*\right)$ . Following our previous work [22], we model the mechanical behaviour of GAG particles using a modified neo-Hookean model with Cauchy stress

$$\sigma_i^{\text{GAG}} = \frac{1}{J_i} \mu^{\text{GAG}} (\mathbf{B}_i - \mathbf{I}) - \Pi \mathbf{I}, \quad (2.27)$$

where  $\mathbf{B}_i = \mathbf{F}_i \mathbf{F}_i^T$  is the left Cauchy–Green tensor and  $\mu^{\text{GAG}} = 0.1 \text{ kPa}$  [22] is a shear modulus, which is significantly smaller than the shear modulus of the arterial media ( $\mu = 89.7 \text{ kPa}$  in table 2).

## 2.7. Smoothed particle hydrodynamics modelling of dissection

To model damage and delamination caused by local swelling of GAGs, the radial stress at the tip of the pool is calculated and compared to a critical value ( $\sigma_{\text{cr}} \sim 61 \text{ kPa}$ , determined via failure tests of the medial layer of the aorta [23]). Once the radial stress exceeds the critical value, the strain energy function defined in equation (2.23) is attenuated in proportion to a damage parameter  $D \in [0, 1]$ , such that the subsequent modified strain energy function is  $(1 - D)W(\mathbf{C}, \mathbf{M}_i^k)$  [24]. Evolution of the damage parameter beyond the critical stress is determined from the radial stretch experienced by the particles,

$$D = \begin{cases} \exp\left(\frac{\Delta\lambda_r}{\tau}\right) - 1 & \sigma \geq \sigma_{\text{cr}}, \\ 0 & \sigma < \sigma_{\text{cr}}, \end{cases} \quad (2.28)$$

where  $\Delta\lambda_r = \lambda_r(\sigma_r > \sigma_{\text{cr}}) - \lambda_r(\sigma_r = \sigma_{\text{cr}})$  is the increase in the radial stretch beyond its critical value and  $\tau$  is a rate parameter (with the condition that  $\tau \geq \Delta\lambda_r / \sqrt{\ln 2}$ ) that regulates growth of the damage parameter with stretch, which is given by a normal distribution such that  $\Delta\lambda_r \approx 5\text{--}10\%$  leads to a complete rupture, defined by  $D = 1$  [9]. Note that the stored energy has a radial contribution from the elastin-dominated matrix alone, thus incorporating a failure criterion in the radial direction that elucidates the separation of the elastic lamellae during medial delamination.

We assume that once a normal particle (elastin, collagen, SMC) is damaged completely, its contribution to the Cauchy stress is replaced with that of a space-filling GAG particle, namely the modified neo-Hookean function defined in equation (2.27). This is accomplished by performing a relaxation step to dissipate oscillations of the converted particles as they reach a stable configuration. Next, we gradually increase the swelling pressure of the new GAG particle and monitor the rise in the radial stress of particles adjacent to the tip of the pool. This process is continued to determine the growth of the GAG pool and the associated delamination within the intra-lamellar space.

## 3. Results

Figure 3*a* shows that the passive mean-behaviour and bi-layered SPH models describe equally well the passive pressure–diameter and associated mean circumferential Cauchy stress–stretch behaviours calculated at a fixed axial stretch ( $\lambda_z = 1.62$ ) agreeing with the analytical thin-walled model, which in turn describes experimental data well [19]. The active model similarly captures well approximately 20% contraction in diameter at the homeostatic pressure (103 mmHg), in agreement with data [21]. Comparing transmural distributions of circumferential Cauchy stress through the wall at a given pressure reveals a fundamental difference between the mean-behaviour and bi-layered models (figure 3*b,c*). While the mean-behaviour model shows the expected highly non-uniform distribution of circumferential stress when neglecting residual stress (figure 3*b*, bottom row), the deposition-stretch based bi-layered model shows the expected near uniform stress in each layer at the homeostatic *in vivo* state, which is thought to be mechanobiologically favourable (figure 3*c*, bottom row, passive). Moreover, the bi-layered model captures the protective role of the adventitia at acutely elevated pressures, which is absent in the mean-behaviour model. That is, in response to pressures above homeostatic ( $P_0 = 103 \text{ mmHg}$ ), undulated collagen fibres in the adventitia straighten and thereby hinder further distension of the arterial wall, resulting in a modest increase in stresses experienced by the elastin-dominated media and a better protection of the embedded passive SMCs. Comparing the circumferential stress for the passive and active models in figure 3*c* (black and grey lines) shows that SMC activation increases load bearing by the media, thus contraction of a vessel at a fixed pressure reduces the circumferential stress in the adventitia.

Next, consider the bi-layered passive and active SPH models and calculated local stress distributions for four different cases of GAG pools having different dimensions, referred to as cases I to IV and defined by increasing angular sectors ( $3^\circ$ ,  $6^\circ$ ,  $10^\circ$  and  $16^\circ$  shown in figure 4*a*) while centred at a common radial position ( $R = 663 \mu\text{m}$ ). These pools also exhibit varying GAG concentrations from 0 to  $150 \text{ mEq l}^{-1}$  (i.e. an approximately 0–95 kPa Gibbs–Donnan swelling pressure). Introducing a GAG pool involves two steps: (i) transforming the material behaviour of a normal medial particle to that of a GAG particle, characterized by a relatively low shear modulus (equation (2.27)), and (ii) increasing its swelling pressure ( $\Pi$  in equation (2.27)) over the simulation. Converting the designated medial particles to GAG particles in the first step increases the compressive radial stress at the tip of the GAGs (figure 4*b,c*, top, at zero GAG concentration) and the tensile hoop stress at the top boundary of the GAGs (figure 4*b,c*, bottom) in proportion to the size of the pool. As the GAGs swell within a pool (i.e. as concentration  $c^{\text{FC}}$  increases), the radial stress at the tip of the pool, predicted by both the passive and active models, transforms from compressive (negative) to tensile (positive) and intensifies with GAG concentration. This specific value of radial stress differs depending on the size of the GAG pool, with smaller pools yielding higher stress concentrations at the tip. Similar increases in stress are observed for the hoop stress at the top boundary. Interestingly, in the passive model, the tensile radial stress observed at high GAG concentrations (at greater than  $75 \text{ mEq l}^{-1}$ ) does not change appreciably in response to increasing intraluminal

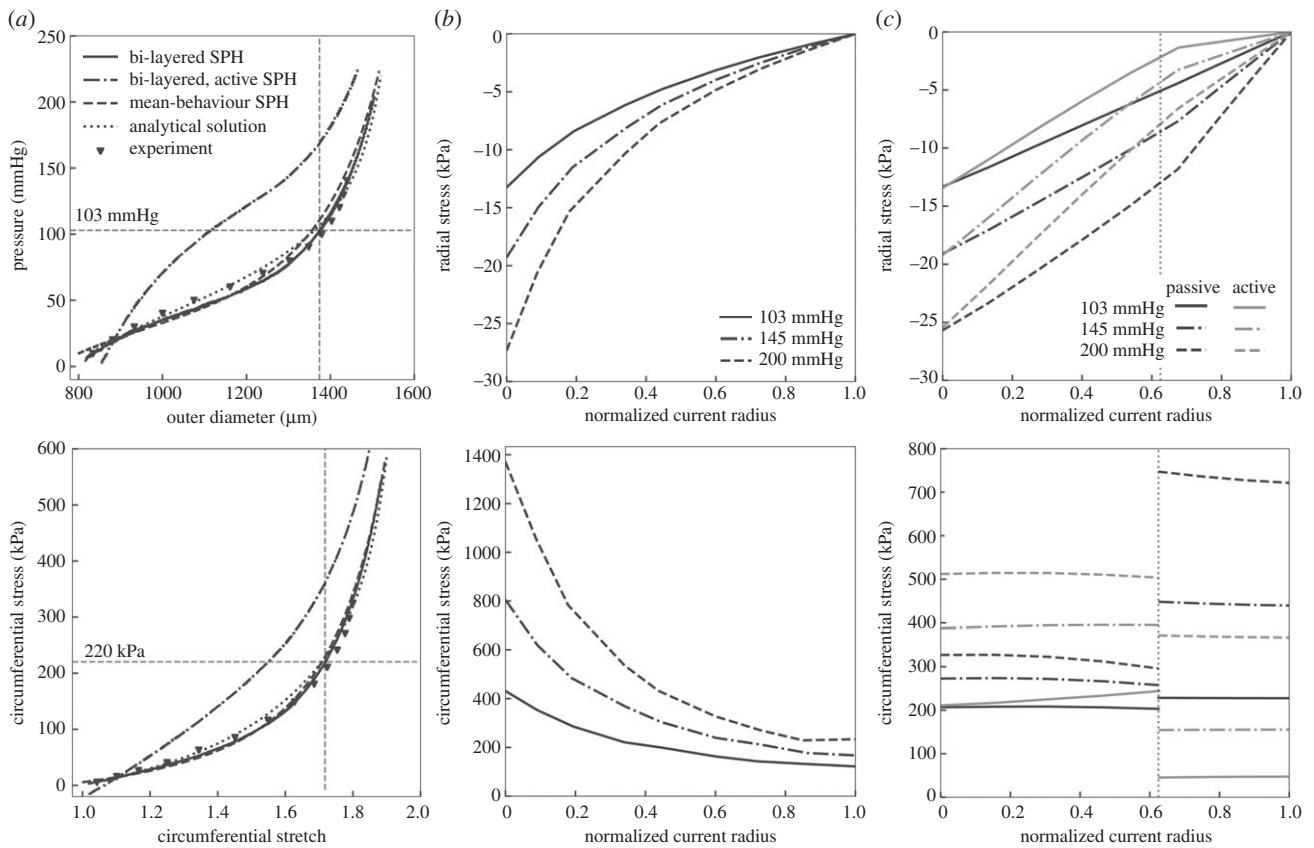


**Figure 3.** Aortic wall stress predicted by the mean-behaviour (§2.4.1) and bi-layered (§2.4.2) SPH models. (a) The pressure–outer diameter (top row) and circumferential stress–stretch (bottom row) behaviours predicted by the mean-behaviour and bi-layered SPH models agree well with the analytical solution, which in turn captures experimental data [14]. The active model further shows the reduction in diameter caused by contracted SMCs, also consistent with data [21]. Horizontal and vertical lines denote the homeostatic configuration. Circumferential stretch is normalized to the traction-free configuration. (b,c) Distribution of the radial (top) and circumferential (bottom) Cauchy stresses predicted by the (b) mean-behaviour and (c) bi-layered models (passive and active) at the homeostatic and two elevated pressures. Dashed vertical line in (c) shows the medial–adventitial border in the bi-layered model. Note that the deposition pre-stretches in the bi-layered model homogenize the circumferential stress by layer and the adventitia stress shields the media at elevated pressures, which is not captured by the mean-behaviour model. Active stresses can similarly off-load stresses otherwise carried by passive constituents.

pressure. This appears to be due to both the Gibbs–Donnan swelling pressure being considerably larger than the radial stress caused by intraluminal pressurization of the wall and the protective role of the adventitia; higher intraluminal pressures in the passive model do not dramatically increase the circumferential or radial stress in the media, and hence do not alter the stress concentration caused by the GAGs.

Comparing results for the passive and active models shows further that vasoconstriction of the vessel and associated thickening of the wall induced by active stresses, especially at lower pressures (103 and 145 mmHg), tend to reduce the radial stress at the tip of the pool. This finding suggests that the SMC contractility may play a protective role against damage and delamination, especially at homeostatic or modestly higher pressures, consistent with experimental findings [4]. On the other hand, the active model shows higher stress concentrations for smaller GAG sizes (cases I and II) at extremely high pressures (200 mmHg). This elevated stress is caused by the large active stress generated by the SMCs and the relatively thin wall at this pressure, which together may hinder swelling of the GAG pool but produce a large stress concentration at its tip. Taken together, these results suggest a marked increase in tensile radial stress near the GAG pools, especially in passive vessels near the homeostatic pressure, which would be expected to increase the vulnerability of the associated

medial region to delamination and possible dissection. Because SMCs are often dysfunctional or absent in thoracic aortic diseases [4,5] and because the higher stress concentrations in the passive model represent the more severe scenario, we focus below on the effects of GAG pools in the absence of SMC contraction.

Figure 5a shows snapshots of the growth of a GAG pool within the media at the homeostatic pressure (103 mmHg) of the passive model. The critical stress associated with failure of medial tissue determines the rate of growth of the pool. Figure 5b shows the radial stress at the tip of the GAG pool as it propagates. Here we test three stress thresholds,  $\sigma_{cr} = 30, 40$  and  $60$  kPa, comparable to the approximately 61 kPa that was determined via failure analysis of porcine thoracic aorta [23], noting that our study is focused on the mouse and the failure stresses examined here may be lower than the porcine models. As seen in figure 5b, and as expected, the rate of GAG propagation decreases with an increase in the critical stress. For example, increases from  $\sigma_{cr} = 30$  kPa to  $60$  kPa reduce the rate of GAG propagation by more than two-fold. Note, too, that the propagation of a single GAG pool is spontaneous; once the radial stress exceeds the critical value, the GAG pool grows catastrophically within the otherwise homogeneous media. Thus, growing GAG pools can potentially reach other accumulations of GAGs and thereby spread throughout the wall.

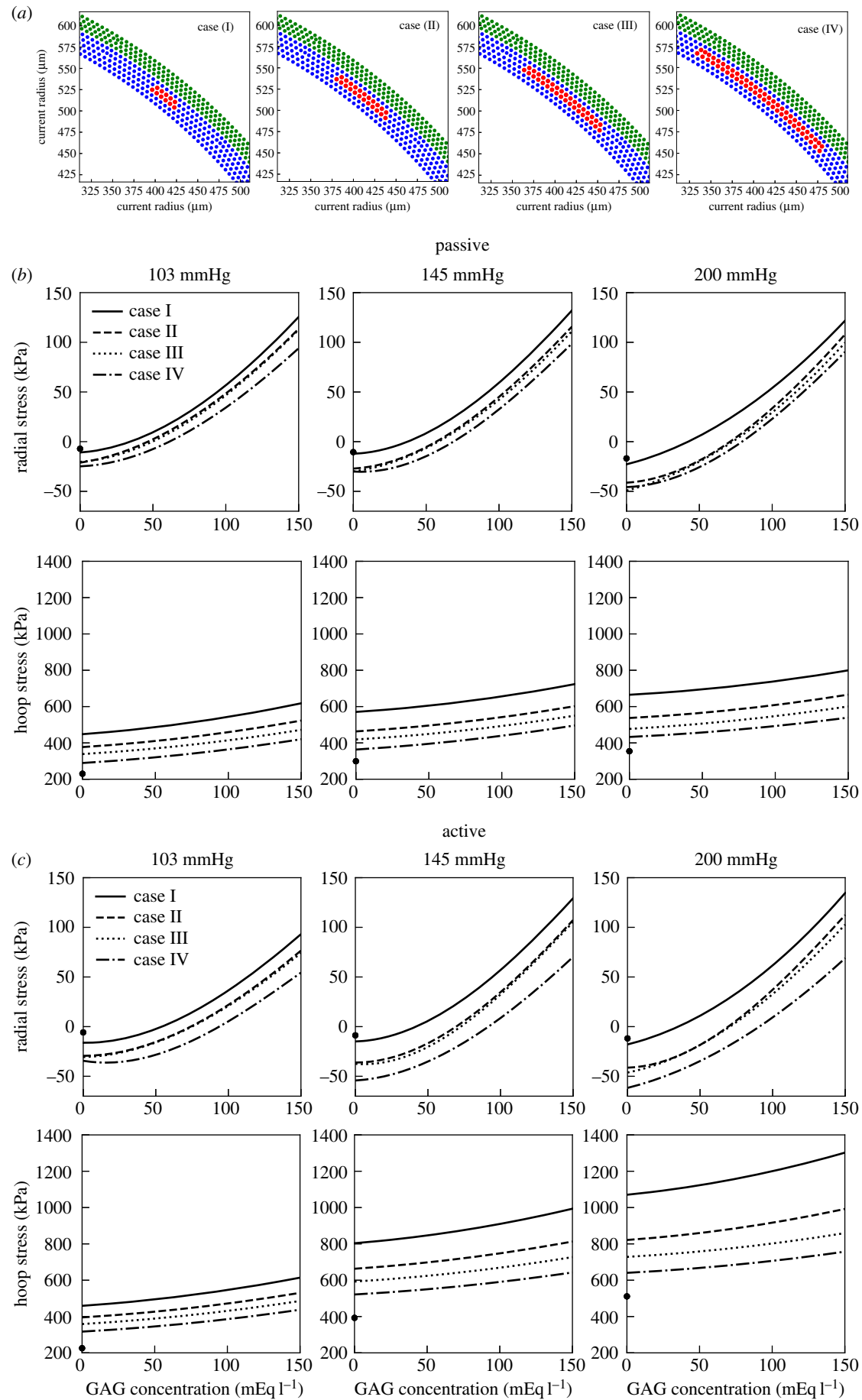


**Figure 4.** Stresses near four different GAG pools placed within the media for three different intraluminal pressures as a function of GAG concentration ( $0\text{--}150\text{ mEq l}^{-1}$ ). (a) Cases corresponding to GAG pools of four different dimensions. Generally, the value of radial stress at the tip of the pool and the hoop (circumferential) stress at the top boundary of the pool predicted by the passive (b) and active (c) models represent stress concentrations that tend to decrease as the pool enlarges. The filled circles on the vertical axes of each plot denote the state of the stress before converting the designated medial particles to GAG particles. Note, in particular, that the radial stresses change from compressive to tensile, typically exceeding approximately  $50\text{ kPa}$  for GAG concentration greater than  $100\text{ mEq l}^{-1}$ .

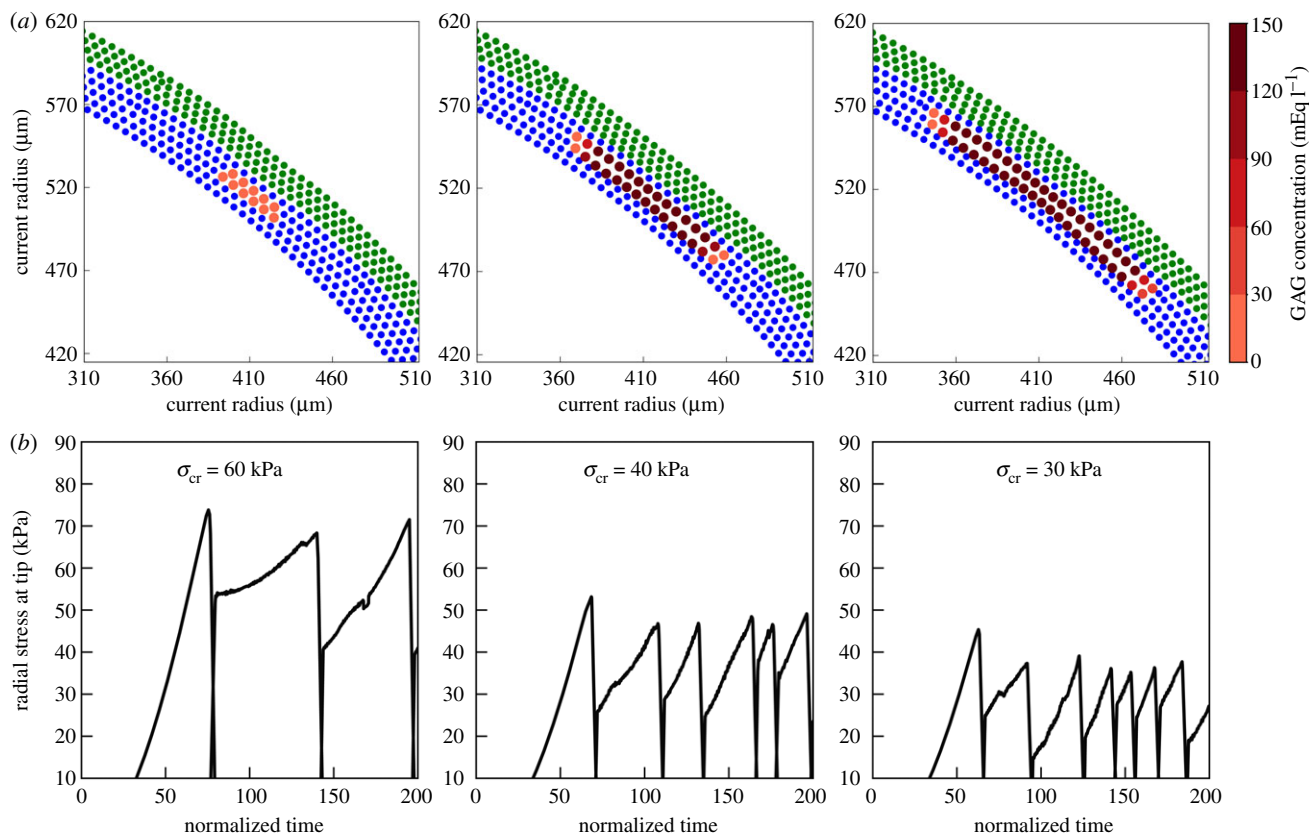


**Figure 5.** Delamination induced by a single GAG pool located within the media in the passive model at the homeostatic pressure. (a) Shown is a progressive delamination for  $\sigma_{cr} = 40$  kPa, starting from the unswollen pool (left), followed by an increase in the GAG concentration and predicted GAG propagation within the intra-lamellar space (middle and right). (b) Shown, too, is the successive rise and drop of radial stress for particles located in front of the pool, with (for illustrative purposes) three different threshold stresses for damage of the tissue ( $\sigma_{cr} = 30, 40$ , or 60 kPa).

To elucidate the possible merging of different GAG pools, we examined interactions between two identical pools that were placed at a given radius within the wall ( $R = 663 \mu\text{m}$ ) but separated to different degrees. Consider two illustrative cases, referred to as ‘low’ and ‘high’ separation (i.e. angular distance between the pools; figure 6). The SPH model predicted that, as GAG concentration increases, the damage and delamination triggered by each pool grows the boundary of the pools in the circumferential direction and eventually leads to coalescence of the pools (figure 6). By determining the number of the damaged medial particles between the two GAGs (referred to as ‘interior’ in figure 6a) or away from the enclosed area (or ‘exterior’), we can determine the rate of GAG propagation in each direction. The model shows that the rate of delamination in the interior region decreases as the pools grow while that in the exterior region increases. These observations are clearer in the high separation configuration; delamination starts and progresses at the same rate in the interior and exterior regions until the internal edges of the pools come into close proximity, after which damage in the interior area slows. Hence, at the onset of coalescence, the extension of each pool in the exterior region is significantly higher than it was in the initial configuration.

We also tested possible interactions between two identical pools that were offset in the radial position (figure 7). This simulation considered the possible coalescence of GAG pools from different intra-lamellar regions. The model shows that the same mechanism underlies the extension and coalescence of two pools of GAGs with or without radial offset. That is, GAG pools appear to have a propensity to merge with

neighbouring GAG pools to form larger accumulations, which have slightly lower values of stress concentration.

## 4. Discussion

We previously used semi-analytical and finite-element-based continuum models to study the effects of diffuse or localized GAGs within the aortic wall [22,25]. Simulations suggested that the normally low, diffuse concentration of GAGs within the medial layer promotes arterial homeostasis by playing key roles in normal mechanotransduction [26]. Importantly, these simulations also supported the hypothesis that pooled GAGs can create significant intramural stress concentrations [6], including a transition from a normally compressive to an unusual tensile stress in the radial direction near the tip of a GAG pool. Although mesh-based models can easily predict such stress concentrations in the vicinity of GAG pools, they are less well-suited to model damage processes that continually decrease stored energy to zero (through  $(1 - D)W(C, M_i^k)$ ) or that progressively convert normal matrix into GAGs and thereby propagate a delamination. By contrast, particle-based methods such as SPH can readily model such processes and, likely, be coupled more easily to particle-based methods that will be needed to describe the flow of blood into a dissection with an associated formation of intramural thrombus (cf. [27]). It is because of the eventual goal of developing coupled fluid–solid–growth models of aortic dissection that the present approach was adopted.

Based on copious findings over the past three decades, detailed models of the arterial wall should also account for

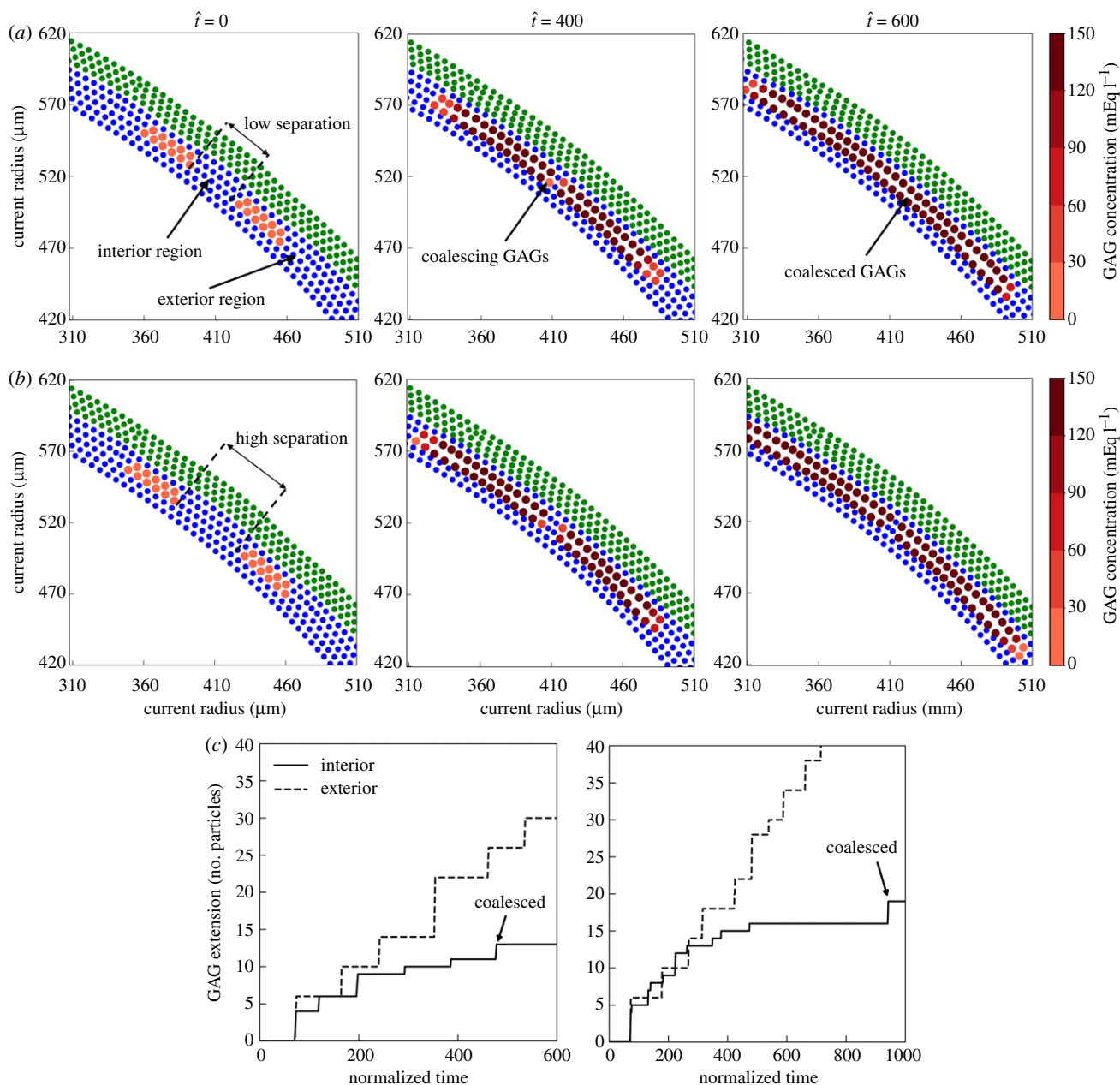


**Figure 6.** Coalescence of two pools of GAGs within the media shown in three snapshots at normalized times  $t = 0, 400$  and  $600$ . Row (a) corresponds to the low separation and (b) to the high separation configurations of the two GAG pools. (c) The number of medial particles converted to GAG particles during growth of the pools in the low separation (left) and high separation (right) configurations. Interior and exterior refer to regions between or away from the GAGs, respectively. The GAG concentration in both pools ranges from 0 to 150 mEq l<sup>-1</sup>. The model predicts that the pools grow in both interior and exterior regions, though the rate of the exterior growth is faster.

its layered structure, residual stresses, axial pre-stress, and baseline anisotropic, nonlinearly elastic material behaviour [28]. Albeit artificial, classical formulations typically prescribe the reference configuration to be an opened, nearly stress-free circular sector, which in turn is deformed into a contiguous traction-free annular configuration to generate the residual stresses. We found such a strategy to be problematic in our Lagrangian-based SPH method and thus adopted a more physiologically relevant approach [15]. We used the *in vivo* homeostatic state as a computationally convenient reference configuration by endowing the individual structurally significant constituents with layer appropriate ‘deposition stretches’ that pre-stress the constituents that self-equilibrate to satisfy local and global equilibrium. This same approach is convenient in studies of arterial growth and remodelling and thus promises to enable the proposed SPH model of the arterial wall to have broader applicability. Indeed, the baseline

SPH model compared favourably with both experimental data and a traditional continuum model in capturing normal murine pressure–diameter and mean stress–stretch behaviours. Moreover, the SPH model also captured the layer-specific transmural distribution of wall stress that was predicted previously using a continuum based model [15]. Given this model verification and validation, we then studied potential effects of GAGs on the aortic mechanics.

Consistent with prior finite-element-based continuum calculations [22], the present SPH model predicted significant stress concentrations at sites of pooled GAGs. As expected, smaller GAG pools were predicted to induce slightly larger stress concentrations than larger pools, with stress magnitude increasing nonlinearly with the concentration of GAG associated fixed charges (from 0 to 150 mEq l<sup>-1</sup>). In contrast to prior continuum-based findings, however, the present results suggest that increasing the luminal pressure, from 103 to

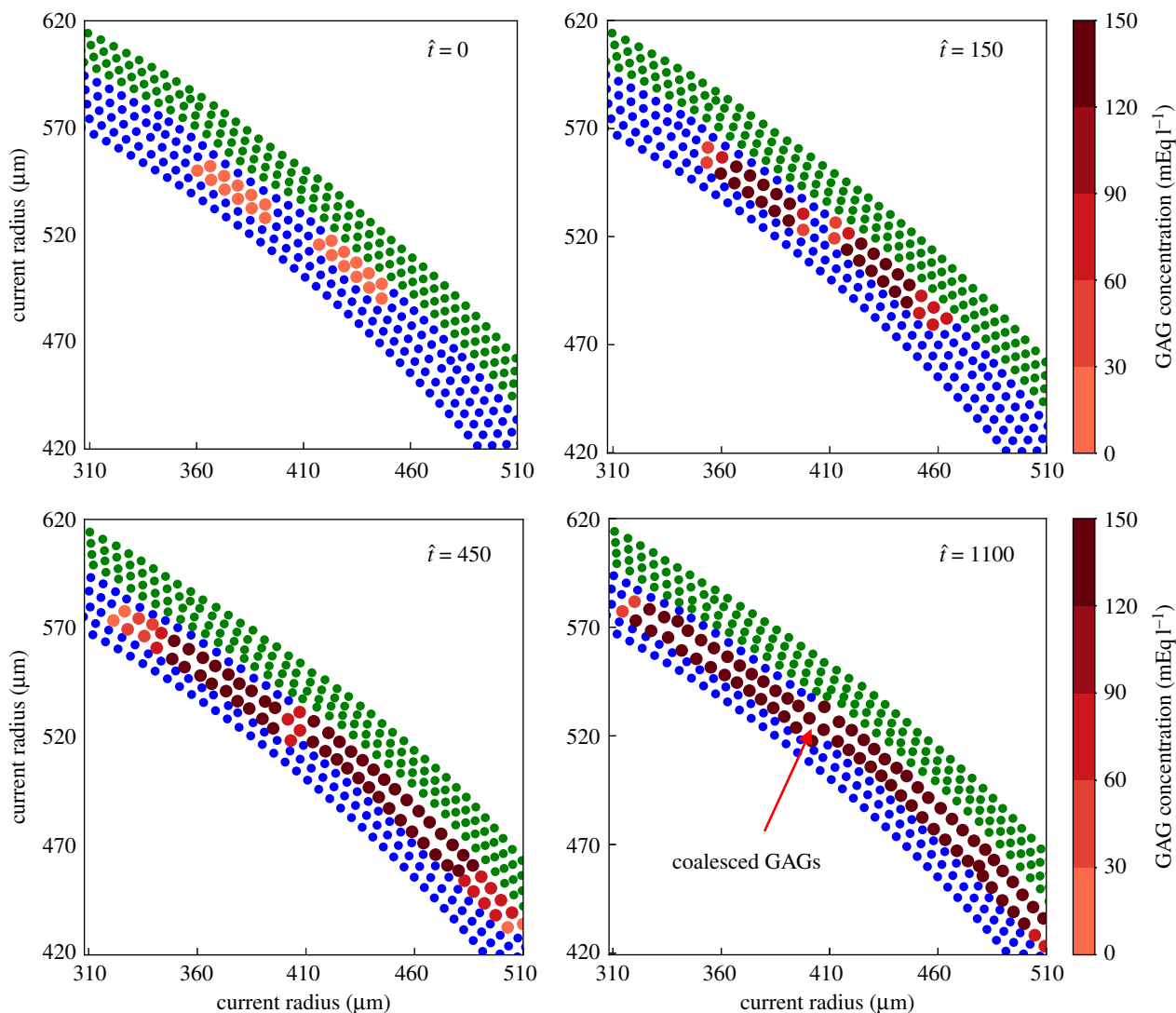


**Figure 7.** Predictions of the SPH model for the coalescence of two GAG pools located at different radial locations. The four snapshots correspond to the progressive delamination from an initial unswollen configuration (upper left) to swollen and eventually merged configurations.

200 mmHg, need not affect the radial stress concentration. Importantly, acute increases in blood pressure have been implicated in aneurysmal dissection/rupture, and patients with particular genetic predispositions are encouraged to avoid strenuous activities such as weight lifting [29]. Hypertension is also a risk factor for dissection [3], though its role is complicated by associated aortic wall remodelling. There are a few possible reasons for this difference in predicted stresses. First, our prior continuum-based models did not include an adventitial layer [22,25], which both a prior semi-analytical [15] and the present SPH model show carries increasingly more of the pressure-load at higher pressures and thus could protect the media. Indeed, SMC activation can similarly be protective by off-loading a vulnerable matrix [4], as confirmed by our simulations. Unfortunately, many cases of aortopathy that lead to dissection involve a loss of function or number of SMCs, which now appears to be additionally detrimental. We thus focused primarily, as we did before, on a passive wall. Second, our prior continuum-based models did not allow possible expansion of the GAG pool as wall stress increases and the wall delaminates; such propagation is central to the biomechanics.

Regardless, the present results suggest for the first time that delamination can progress within a medial layer as stresses build up and then drop as the pool expands, only to

potentially build up again and repeat (figure 5). This process is not unlike that seen in peeling tests on aortic samples [30]. Overall, our simulations also suggested that multiple GAG pools can coalesce to form larger pools whether located within the same or a neighbouring radial location, effectively delaminating the wall further despite the pools tending to grow away from one another more easily than towards one another. Importantly, human histopathological samples show that GAG accumulation often occurs in the presence of damaged or lost elastic laminae, which could also facilitate a progressive GAG coalescence even though this specific scenario was not modelled herein. Taken together, our computational findings strongly support prior studies based on histochemistry that pooled GAGs can be initiators of intramural delaminations that drive aortic dissection [6,7].

There are, of course, a number of extensions to the model that must be realized before the actual process of dissection can be quantified with confidence, extensions that will require additional experimental information. In particular, there is a need to model the ‘musculo-elastic’ units of the media [31–33], meaning the nearly concentric elastic laminae that enclose the SMCs, collagen and GAGs. Such an extension would allow us to consider cases wherein damage to or loss of elastic laminae may facilitate the propagation of delamination and influence its course. Similarly, there is a need to

delineate local properties (e.g. inner versus outer curvature of the ascending aorta [34]) and especially properties in different mutations or states of disease progression [35], noting that dissections often occur in the presence of aneurysms and thus different degrees of medial degeneration. Such properties must include stiffness and strength [36], the latter of which is seldom measured though fundamental to understanding dissection and rupture. Even more important, and difficult, is the need to quantify focal geometric and material heterogeneities within the wall, which are likely key in initiating delaminations and controlling their propagation, particularly inward to the luminal surface (to create a false lumen) or outward (to cause rupture). Much remains to be accomplished, with computational tools expected to advance as additional biological complexities are discovered, with mouse models continuing to provide insight despite inherent differences between murine and human conditions. There is also a pressing need for coupled models that can account for the dissection of the wall, the inflow and clotting of blood, and the subsequent maturation of the thrombus and growth and remodelling of the injured wall. We submit that continuum-particle-based approaches may facilitate such fluid–solid–growth modelling of aortic dissection.

In conclusion, the present results provide independent confirmation of prior simulations that pooled GAGs within the aortic media can generate sufficient local Gibbs–Donnan swelling pressures to propagate delaminations within the

media. Whereas most experimental studies of dissection potential have focused on mode I peeling tests [30,37], there is a pressing need for combined experimental–computational studies of heterogeneities within the compromised thoracic aorta to determine if and how intramural delaminations can cross (damaged) elastic laminae and either create an intimal defect and associated false lumen or cause catastrophic rupture. That is, whereas the majority of prior biomechanical assessments of aortic mechanical properties have focused on transmurally averaged properties, even if within different layers, there is a pressing need for information on the expected intramural heterogeneities that render the diseased aortic wall susceptible to dissection and rupture.

**Data accessibility.** The SPH code is deposited in [https://github.com/Hossein-Upenn/SPH\\_Arterial\\_Delamination\\_HA](https://github.com/Hossein-Upenn/SPH_Arterial_Delamination_HA).

**Authors' contributions.** H.A., M.K.R. and J.D.H. designed the study. H.A. developed the computational model and performed the simulations. All authors interpreted the results and drafted the manuscript.

**Competing interests.** We declare we have no competing interests.

**Funding.** This work was supported by grants from the US NIH: U01 HL116323 and U01 HL142518 (to J.D.H. and G. Karniadakis), P01 HL134605 (D. Rifkin, J.D.H. and G. Tellides Project 4 Leads) and R21 EB020968 (to J.D.H.).

**Acknowledgements.** We are very thankful to Prof. George Karniadakis for his critical advice on and assessment of the details of the SPH model.

## References

- Roberts WC. 1981 Aortic dissection: anatomy, consequences, and causes. *Am. Heart J.* **101**, 195–214. (doi:10.1016/0002-8703(81)90666-9)
- Hagen PG, Nienaber CA, Isselbacher EM, Bruckman D, Karavite DJ, Russman PL. 2000 The international registry of acute aortic dissection. *JAMA* **283**, 897–903. (doi:10.1001/jama.283.7.897)
- Evangelista A *et al.* 2018 Insights from the international registry of acute aortic dissection: a 20-year experience of collaborative clinical research. *Circulation* **137**, 1846–1860. (doi:10.1161/CIRCULATIONAHA.117.031264)
- Ferruzzi J, Murtada S-I, Li G, Jiao Y, Uman S, Ting MYL, Tellides G, Humphrey JD. 2016 Pharmacologically improved contractility protects against aortic dissection in mice with disrupted transforming growth factor- $\beta$  signaling despite compromised extracellular matrix properties. *Arterioscler. Thromb. Vasc. Biol.* **36**, 919–927. (doi:10.1161/ATVBAHA.116.307436)
- Bellini C, Wang S, Milewicz DM, Humphrey JD. 2015 Myh 11<sup>R247C/R247C</sup> mutations increase thoracic aorta vulnerability to intramural damage despite a general biomechanical adaptivity. *J. Biomech.* **48**, 113–121. (doi:10.1016/j.jbiomech.2014.10.031)
- Humphrey JD. 2013 Possible mechanical roles of glycosaminoglycans in thoracic aortic dissection and associations with dysregulated transforming growth factor- $\beta$ . *J. Vasc. Res.* **50**, 1–10. (doi:10.1159/000342436)
- Cikach FS *et al.* 2018. Massive aggrecan and versican accumulation in thoracic aortic aneurysm and dissection. *JCI Insight* **3**, e97167. (doi:10.1172/jci.insight.97167)
- Azeloglu EU, Albro MB, Thimmappa VA, Ateshian GA, Costa KD. 2008 Heterogeneous transmural proteoglycan distribution provides a mechanism for regulating residual stresses in the aorta. *Am. J. Physiol. Heart Circ. Physiol.* **294**, H1197–H1205. (doi:10.1152/ajpheart.01027.2007)
- Rausch MK, Karniadakis GE, Humphrey JD. 2016 Modeling soft tissue damage and failure using a combined particle/continuum approach. *Biomech. Model. Mechanobiol.* **16**, 249–261. (doi:10.1007/s10237-016-0814-1)
- Desbrun M, Gascuel M-P. 1996 Smoothed particles: a new paradigm for animating highly deformable bodies. In *Computer animation and simulation '96* (eds R Boulic, G Hégon), pp. 61–76. Vienna, Austria: Springer. (doi:10.1007/978-3-7091-7486-9\_5)
- Ganzenmüller GC, Sauer M, May M, Hiermaier S. 2016 Hourglass control for smooth particle hydrodynamics removes tensile and rank-deficiency instabilities. *Eur. Phys. J. Spec. Top.* **225**, 385–395. (doi:10.1140/epjst/e2016-02631-x)
- Randles PW, Libersky LD. 1996 Smoothed particle hydrodynamics: some recent improvements and applications. *Comput. Methods Appl. Mech. Eng.* **139**, 375–408. (doi:10.1016/S0045-7825(96)01090-0)
- Ferruzzi J, Bersi MR, Humphrey JD. 2013 Biomechanical phenotyping of central arteries in health and disease: advantages of and methods for murine models. *Ann. Biomed. Eng.* **41**, 1311–1330. (doi:10.1007/s10439-013-0799-1)
- Bersi MR, Bellini C, Wu J, Montaniel KRC, Harrison DG, Humphrey JD. 2016 Excessive adventitial remodeling leads to early aortic maladaptation in angiotensin-induced hypertension. *Hypertension* **67**, 890–896. (doi:10.1161/HYPERTENSIONAHA.115.06262)
- Bellini C, Ferruzzi J, Roccabianca S, Di Martino ES, Humphrey JD. 2014 A microstructurally motivated model of arterial wall mechanics with mechanobiological implications. *Ann. Biomed. Eng.* **42**, 488–502. (doi:10.1007/s10439-013-0928-x)
- Chuong CJ, Fung YC. 1986 Residual stress in arteries. In *Frontiers in biomechanics*, pp. 117–129. New York, NY: Springer.
- Li K, Ogden RW, Holzapfel GA. 2017 An exponential constitutive model excluding fibres under compression: application to extension–inflation of a residually stressed carotid artery. *Math. Mech. Solids* **23**, 1081286517712077. (doi:10.1177/1081286517712077)
- Cardamone L, Valentin A, Eberth JF, Humphrey JD. 2009 Origin of axial prestretch and residual stress in arteries. *Biomech. Model. Mechanobiol.* **8**, 431. (doi:10.1007/s10237-008-0146-x)
- Latorre M, Humphrey JD. 2018 Modeling mechano-driven and immuno-mediated aortic maladaptation

- in hypertension. *Biomech. Model. Mechanobiol.* **17**, 1497–1511. (doi:10.1007/s10237-018-1041-8)
20. Rachev A, Hayashi K. 1999 Theoretical study of the effects of vascular smooth muscle contraction on strain and stress distributions in arteries. *Ann. Biomed. Eng.* **27**, 459–468. (doi:10.1114/1.191)
  21. Murtada S-I, Ferruzzi J, Yanagisawa H, Humphrey JD. 2016 Reduced biaxial contractility in the descending thoracic aorta of fibulin-5 deficient mice. *J. Biomech. Eng.* **138**, 051008. (doi:10.1115/1.4032938)
  22. Roccabianca S, Ateshian GA, Humphrey JD. 2014 Biomechanical roles of medial pooling of glycosaminoglycans in thoracic aortic dissection. *Biomech. Model. Mechanobiol.* **13**, 13–25. (doi:10.1007/s10237-013-0482-3)
  23. MacLean NF, Dudek NL, Roach MR. 1999 The role of radial elastic properties in the development of aortic dissections. *J. Vasc. Surg.* **29**, 703–710. (doi:10.1016/S0741-5214(99)70317-4)
  24. Simo JC, Ju JW. 1987 Strain- and stress-based continuum damage models—II. Computational aspects. *Int. J. Solids Struct.* **23**, 841–869. (doi:10.1016/0020-7683(87)90084-9)
  25. Roccabianca S, Bellini C, Humphrey JD. 2014 Computational modelling suggests good, bad and ugly roles of glycosaminoglycans in arterial wall mechanics and mechanobiology. *J. R. Soc. Interface* **11**, 20140397. (doi:10.1098/rsif.2014.0397)
  26. Humphrey JD, Schwartz MA, Tellides G, Milewicz DM. 2015 Role of mechanotransduction in vascular biology: focus on thoracic aortic aneurysms and dissections. *Circ. Res.* **116**, 1448–1461. (doi:10.1161/CIRCRESAHA.114.304936)
  27. Yazdani A, Li H, Bersi MR, Di Achille P, Insley J, Humphrey JD, Karniadakis GE. 2018 Data-driven modeling of hemodynamics and its role on thrombus size and shape in aortic dissections. *Sci. Rep.* **8**, 2515. (doi:10.1038/s41598-018-20603-x)
  28. Humphrey JD, Rajagopal KR. 2002 A constrained mixture model for growth and remodeling of soft tissues. *Math. Models Methods Appl. Sci.* **12**, 407–430. (doi:10.1142/S0218202502001714)
  29. Hatzaras I, Tranquilli M, Coady M, Barrett PM, Bible J, Elefteriades JA. 2007 Weight lifting and aortic dissection: more evidence for a connection. *Cardiology* **107**, 103–106. (doi:10.1159/000094530)
  30. Tong J, Cheng Y, Holzapfel GA. 2016 Mechanical assessment of arterial dissection in health and disease: advancements and challenges. *J. Biomech.* **49**, 2366–2373. (doi:10.1016/j.jbiomech.2016.02.009)
  31. Clark JM, Glagov S. 1985 Transmural organization of the arterial media. The lamellar unit revisited. *Arteriosclerosis* **5**, 19–34. (doi:10.1161/01.ATV.5.1.19)
  32. O'Connell MK *et al.* 2008 The three-dimensional micro- and nanostructure of the aortic medial lamellar unit measured using 3D confocal and electron microscopy imaging. *Matrix Biol.* **27**, 171–181. (doi:10.1016/j.matbio.2007.10.008)
  33. Tsamis A, Pal S, Phillippi JA, Gleason TG, Maiti S, Vorp DA. 2014 Effect of aneurysm on biomechanical properties of 'radially-oriented' collagen fibers in human ascending thoracic aortic media. *J. Biomech.* **47**, 3820–3824. (doi:10.1016/j.jbiomech.2014.10.024)
  34. Tsamis A *et al.* 2016 Extracellular matrix fiber microarchitecture is region-specific in bicuspid aortic valve-associated ascending aortopathy. *J. Thorac. Cardiovasc. Surg.* **151**, 1718–1728.e5. (doi:10.1016/j.jtcvs.2016.02.019)
  35. Bersi MR, Bellini C, Humphrey JD, Avril S. In press. Local variations in material and structural properties characterize murine thoracic aortic aneurysm mechanics. *Biomech. Model. Mechanobiol.* (doi:10.1007/s10237-018-1077-9)
  36. Thunes JR, Phillippi JA, Gleason TG, Vorp DA, Maiti S. 2018 Structural modeling reveals microstructure-strength relationship for human ascending thoracic aorta. *J. Biomech.* **71**, 84–93. (doi:10.1016/j.jbiomech.2018.01.037)
  37. Pal S, Tsamis A, Pasta S, D'Amore A, Gleason TG, Vorp DA, Maiti S. 2014 A mechanistic model on the role of 'radially-running' collagen fibers on dissection properties of human ascending thoracic aorta. *J. Biomech.* **47**, 981–988. (doi:10.1016/j.jbiomech.2014.01.005)